# Processing of Nano-Sized Boron Carbide Powder

A Thesis
Presented to
The Academic Faculty

by

**Kathleen Silver**

In Partial Fulfillment
of the Requirements for the Degree
Master of Science in Materials Science and Engineering

School of Materials Science and Engineering
Georgia Institute of Technology
December 2007

# Processing of Nano-Sized Boron Carbide Powder

Approved by:

Dr. Robert F. Speyer, Advisor
School of Materials Science and Engineering
*Georgia Institute of Technology*

Dr. Thomas H. Sanders, Jr.
School of Materials Science and Engineering
*Georgia Institute of Technology*

Dr. Elizabeth Judson
General Manager, Verco Materials, LLC

Date Approved: August 20, 2007

# ACKNOWLEDGEMENTS

My path to a master's degree has been both challenging and exciting. I could not have successfully navigated the journey without the help of many, many people. I am very appreciative of Dr. Robert Speyer's willingness to lead me on this journey to a master's degree and I will always remember the help his grad students showed me. I am especially grateful to Dr. Namtae Cho who has been a true mentor and leader throughout this process. I'm equally indebted to Dr. Elizabeth Judson and Dr. Thomas Sanders, who served on my committee; to my undergraduate advisor, Dr. Brent Carter and to all the MSE faculty and staff, who each at the most important of times, came through for me with unwavering support.

This work was made possible through the support of Georgia Research Alliance Technology Partnership funding administered through the Georgia Tech Enterprise Innovation Institute's VentureLab program.

I've often said my degree should contain many additional names, for many people have helped me achieve this goal. If there were room on the degree, the entire Peachtree Corners neighbor list would be included for their support of my family and me and for their willingness to "be the village" that helped raise my kids during the extended, time consuming period during which I pursued my collegiate dream. Finally, there are no words to express my appreciation to my children, Sarah and Benjamin and their father and my husband, Martin. They let me lock myself in my room to study whenever necessary; they endured several years of frozen dinners and macaroni & cheese and they put up with many other inconveniences so I could achieve this dream.

Thank you to one and all!

# TABLE OF CONTENTS

# LIST OF TABLES

# LIST OF FIGURES

# SUMMARY

Because boron carbide is extremely hard with a low theoretical density, it is an excellent material for military armor. Recent studies indicate $B_4C$ nanopowder may provide additional advantages without loss of established properties. In this study, preliminary forms of graphite-coated $B_4C$ nanopowders with various additives were sintered and analyzed. A fine-grained powder on the order of 20-40 nm was supplied by PPG Industries. These powders were then mixed with other additives such as Al, Fe and Ti. Methanol washing was performed on the powders to remove most of the $B_2O_3$ impurity usually present. XRD analysis of the powders verified the nanograined nature and, to some extent, the amount of amorphous material within the powders. A dilatometer furnace was used to track the dimensional changes during sintering, and densities of sintered samples were compared to green compact densities. The onset of sintering occurred at various temperatures depending on the dopant and its amount, most often occurring at higher temperatures than expected. This was likely due first to volatilization of residual $B_2O_3$ and then to the graphite coatings of the powders preventing direct $B_4C$-$B_4C$ contact. Double-stage sintering, where sintering is either slowed, arrested or reversed and then re-accelerated, occurred in all but one sample. Samples with sintered densities greater than 93% theoretical density were hot isostatically pressed (HIP) with the expectation that the post-HIP density would be 100% theoretical density. Ultimately, post-HIP densities increased less than 2% compared to sintered densities.

# CHAPTER 1

## Introduction

Boron carbide is the third hardest material next to diamond and cubic boron nitride. In addition to having a Knoop hardness of 2800 kg/mm$^2$, using a 100 g load [1], it is lightweight (theoretical density: 2.52 g/cm$^3$) and has a 4-point bending strength of at least 300 MPa [2], making it an excellent material for personal armor. It has a high melting point (2450°C), high neutron absorption cross-section, and is resistant to chemical agents [3]. These properties make it useful in nuclear shielding applications. It also has excellent abrasion resistance making it useful as a nozzle material for slurry pumping and grit blasting [3].

Bonding of boron carbide is essentially covalent with a covalent bond energy of 9.42 eV and an ionic bond energy of 1.41 eV [4]. Its crystal structure consists of an icosahedron with twenty faces and twelve equivalent vertices that form a twelve atom cage (see Figure 1.1). These icosahedra are centered about each corner of a rhombohedron. They are directly bonded to six other icosahedra and are also connected via a three atom chain running through the rhombohedra [5]. This configuration leads to a space group classification of R3m. Due to binding constraints, carbon can only occupy two of the twelve icosahedral positions. However, boron substitution in the chains or at interstitial positions leads to a wide range of homogeneity in the solid state (8.8 to 20 mol% carbon) [3], as shown in Figure 1.2. In addition to ($B_{11}C$)CBC (equivalent to $B_4C$), ($B_{12}$)CBC (equivalent to $B_{13}C_2$) and other higher boron compositions can exist [4].

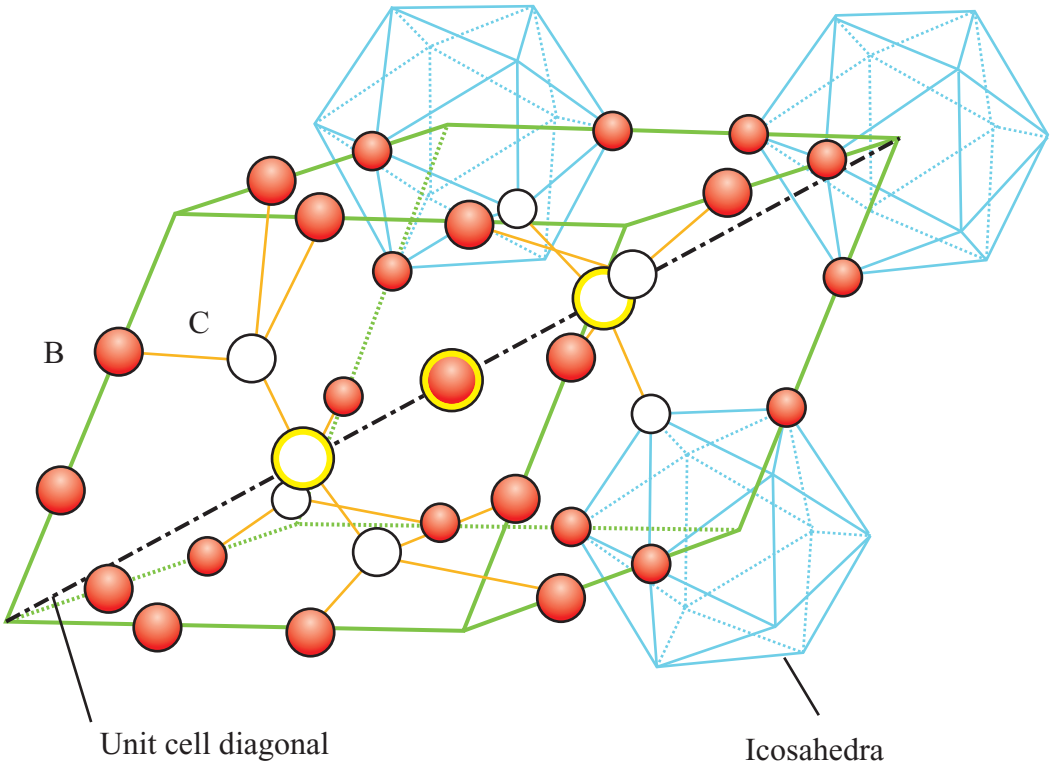


**Fig** 1.1: Crystal structure of boron carbide [3].

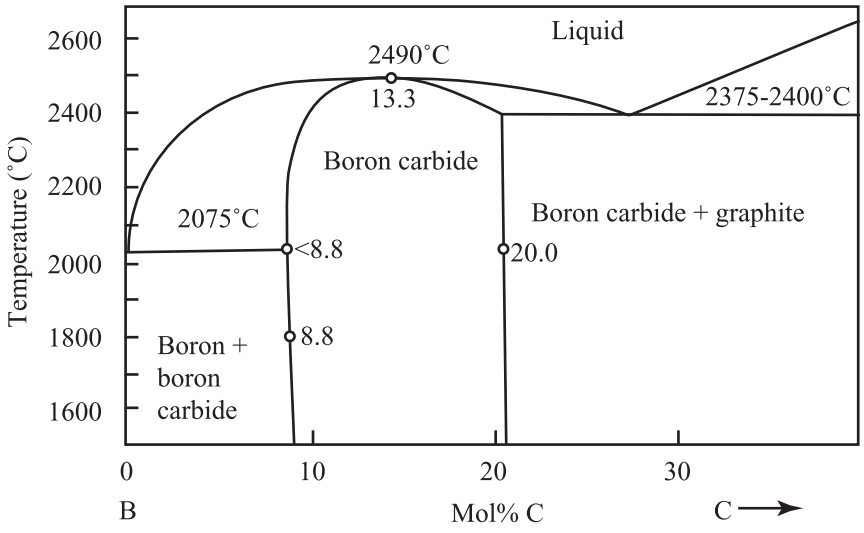


**Fig** 1.2: Boron carbide phase diagram [3].

High hardness combined with high fracture toughness are requisites for effective ballistic materials [6, 7]. When a projectile impacts a ceramic ballistic material, a compressive shock wave is created which extends hemispherically from the impact point. This shock wave generates tensile tangential stresses which then cause the formation of radial cracks eminating from the impact point. Due to these tangential stresses, cracks preferentially open at the sites of pores and fissures. Therefore, ballistic performance improves with decreasing porosity, i.e. with increased sintered relative density [8].

Historically, boron carbide has not been known to sinter well due to its strong covalent bonding, low plasticity, high resistance to grain-boundary sliding, and low superficial tension in the solid state. The strong covalent bonding results in slow self-diffusion which inhibits densification by solid-state sintering techniques [3]. Sintering aids such as Si, $Al_2O_3$, Mg, and Fe have been used to increase pressureless sintered density via liquid phase sintering [9]. Yet, these sintering additives often have deleterious effects on mechanical properties [10, 11, 12, 13]. Until recently, hot pressing has been the only method of achieving parts that are near to 100% of theoretical density. However, hot pressing is limited in that it can only economically produce parts that are flat or nearly flat.

Recently, work was performed in our lab [14] to determine the causes of limited densification during pressureless sintering; methods were then developed to overcome these obstacles. It was determined that the presence of $B_2O_3$ coatings on $B_4C$ particles inhibited densification and facilitated particle coarsening. Soaking samples in a hydrogen atmosphere at 1300°C extracted the boron oxide coatings. This permitted direct $B_4C$-$B_4C$ particle contact which caused densification to begin at lower temperatures. A secondary coarsening mechanism was attributed to an increased vapor pressure of $B_4C$ causing evaporation from small particles and condensation on large particles [8]. Overcoming these obstacles allowed for $B_4C$ powder, with particle size of $\sim$1 $\mu$m, to be sintered to $\sim$96% of theoretical density and with hardness values similar to hot pressed samples. Hot isostatic pressing (HIPing) of these dense parts resulted in an increase to 100% of theoretical density and a substantial increase in hardness (see Figure 1.3).

These results and recent information on sintering nanopowder ceramics prompted an

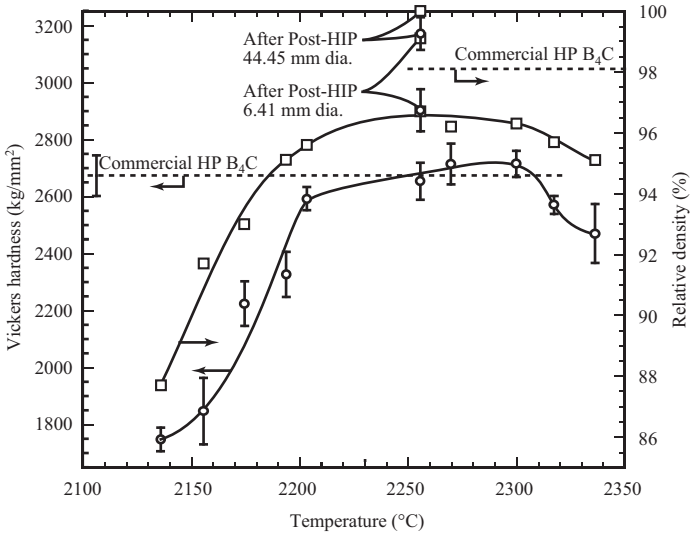


**Fig** 1.3: Vickers hardness of sintered and post-HIPed $B_4C$ as a function of soaking temperature compared to hot pressed sample.

interest in studying nano-sized $B_4C$ powder. The study of nano-sized ceramic materials has grown rapidly in the last decade [15]. Deformation assisted densification techniques via dislocational plasticity are not possible in nanocrystals, but other deformational mechanisms such as grain boundary sliding may become active [16]. Theoretically, nanopowder is highly active due to its greater surface area which should result in a higher driving force for densification [16]. High total surface energy coupled with shortened diffusion distances should enhance sinterability at lower temperatures [17, 18] and improve sintered density. Increased surface area also has drawbacks such as formation of agglomerates that result in lower packing density and increased susceptibility to surface contamination. Surfactants added to the powder suspension to modify the surface have been successful in overcoming these drawbacks [19].

Initial nanopowder research focused on oxide ceramics such as $TiO_2$ or $ZrO_2$. Oxide ceramics with grain sizes of about 50 nm have been pressureless sintered to 95% of theoretical density [19]. The same results have been difficult to achieve with non-oxide ceramics. One reason for this behavior may be the easy oxygen contamination of nano-sized powder surfaces. Oxide formation on powder surfaces hinders densification due to the volatile nature of these oxides that promote grain growth [15]. Avoiding grain growth is important

because most ceramics, including boron carbide, follow a Hall Petch relationship: strength increases as the square root of grain size decreases [20]. This relationship has been observed in the $TiO_2$ system with grain sizes less than 200 nm [19]. In addition to improved strength and hardness resulting from nanophase powders, evidence of superplasticity exists for theoretically dense microstructures that have maintained nanograin size [21, 22].

In this study the sintering reaction behaviors of an early-stage version of nanoscale $B_4C$ powder was evaluated. By combining the knowledge gained in the previous work within our lab with emerging knowledge of sintering nano-phase non-oxide ceramics, it is hoped that the groundwork is laid for developing and processing $B_4C$ nanopowder for armor and wear-resistant applications.

# CHAPTER 2

## Experimental Procedure

As-received boron carbide nanopowders (PPG Industries, Inc., Pittsburgh, PA) with a size range of 20-40 nm were ultrasonicated (FS-14 Solid State Ultrasonicator, Fisher Laboratory Equipment Division, Pittsburgh, PA) for 1 minute in a methanol suspension. The suspension was placed in an 80°C oven for 12 hours to dry thoroughly. This process was repeated three times to remove excess boron oxide from the powders.

X-ray diffraction data (PANalytical XPert PRO x-ray diffractometer, Natick, MA) was obtained with a scan speed of 1 s/step and step size of 0.005° from 10 to 85° $2\theta$. Phase identification was based on the International Center for Diffraction Data (ICDD, Newton Square, PA) database.

Loose powder was placed in a die and punch assembly (Model No. 3925, Carver, Inc., Wabash, IN) and pressed at 300 MPa to produce powder compacts with a green density greater than 60% of theoretical in the form of cylindrical pellets 6.44 mm in diameter and ∼5 mm in height.

Sintering was done in a dilatometric furnace (1000-2560 FP, Thermal Technology, Inc., Santa Rosa, CA) containing graphite heating elements and fibrous insulation. The dilatometer (Theta Industries, Inc., Port Washington, NY) uses a double-pushrod and casing made of graphite (Poco Graphite Inc., Decatur TX) that extends into the furnace and uses a linear variable differential transformer (LVDT) position transducer to measure expansion/contraction in the samples. A counterweight is applied to the sample pushrod to avoid any particle sliding within the powder compact that might result from the force of the pushrod.

Temperature was monitored via an infrared pyrometer (MAISC, Raytek Co., Santa

Cruz, CA) sighted on the samples through the graphite casing. Measurement at a wavelength of 1.0 $\mu$m was conducted through a fused silica viewing port mounted on the side wall of the furnace. Calibration of the pyrometer was based on the allotropic transformations of a pressed compact of high-purity (99.99+%) iron (Sigma-Aldrich, St. Louis, MO) and the polymorphic transformation of high-purity (99.99%) $ZrO_2$ (Aldrich, St. Louis, MO) as well as direct comparison with a wire thermocouple up to 1900°C.

After evacuating the furnace and backfilling with helium two times, samples were heated under flowing helium (5.7 l/h) to 2300 or 2400°C at 10°C/min and soaked at this temperature until shrinkage was less than 0.005%/min. After cooling at 50°C/min to room temperature in helium flowing at 56.7 l/h, geometrical and Archimedes densities were obtained for the samples.

# CHAPTER 3

# Results

## *3.1 Undoped Boron Carbide Powder*

### 3.1.1 Powder Analysis

All undoped powder was purified as shown in Table 3.1.

**Tab** 3.1: Powder Description of Samples #1 - #2

| Sample # | Description |
|---|---|
| 1 | $B_4C$, 98% C, purified, methanol washed |
| 2 | $B_4C$, 98% C, purified, high crystalline |

$B_4C$ was identified as the main phase and graphite was identified as a secondary phase as shown in Figure 3.1. Both patterns exhibit $B_4C$ peak broadening, indicative of nano-sized powder. After methanol washing, $B_2O_3$ remained in both samples. There are unknown peaks at $\sim 18^\circ$ in both samples and also at $\sim 27.5^\circ$ in sample #1. These peaks may be silicon tetraboride ($SiB_4$) and quartz ($SiO_2$) and are thought to be introduced by contamination during powder processing.

### 3.1.2 Sintering Behavior

Both samples displayed double-stage sintering as shown in Figure 3.2. Shrinkage onset began at 1800°C for sample #1 and at 1600°C for sample #2. A plateau occurred at 2050°C for sample #1 and at 1950°C for sample #2. Sintering re-accelerated at 2200°C for both samples. Both samples were soaked at 2300°C for 90 minutes and the resulting net shrinkage was 2% for sample #1 and 0% for sample #2. Sample #2 experienced a large expansion at low temperature.

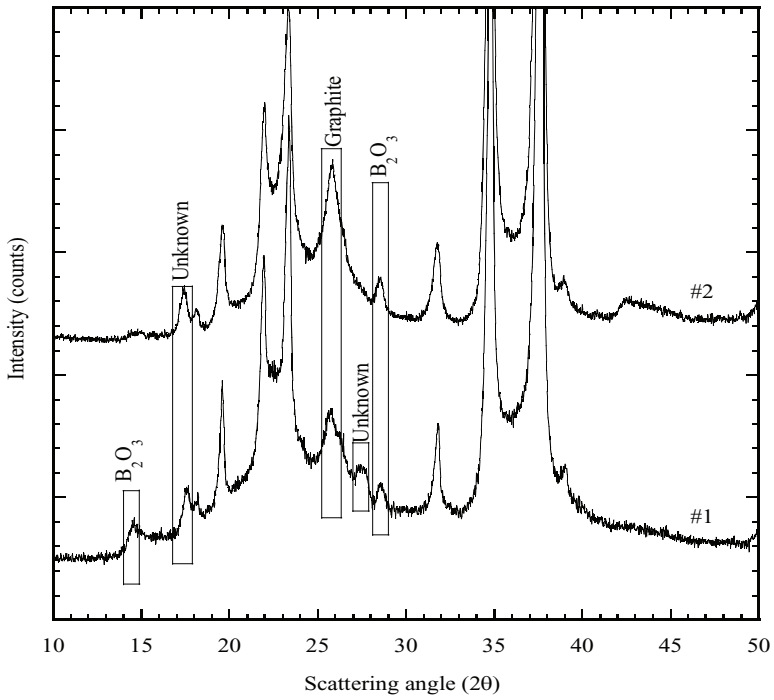


**Fig** 3.1: XRD peaks of undoped PPG powders.

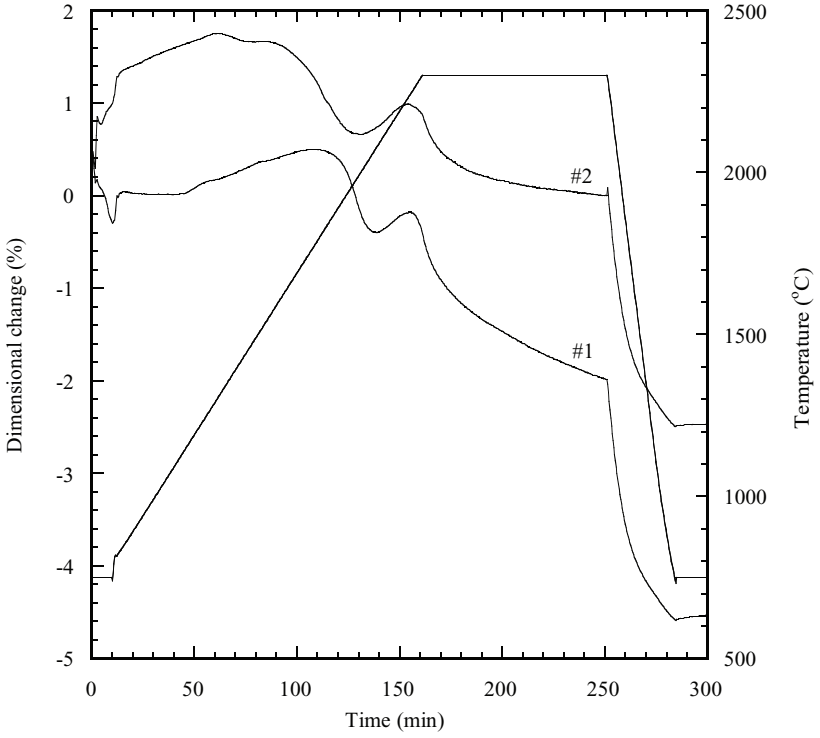


**Fig** 3.2: Dilatometer traces of undoped PPG powders.

### 3.1.3 Density and Weight Loss

Green density, geometrical and Archimedes densities of sintered pellets and the weight losses resulting from sintering are indicated in Table 3.2. The large difference between geometric and Archimedes density for sample #2 is due to a large radial crack in the sintered pellet.

**Tab** 3.2: Relative Density and Weight Loss of PPG #1 - #2.

| Sample number | Green density (%) | Geometrical density (%) | Archimedes density (%) | Weight loss (%) |
|---|---|---|---|---|
| 1 | 69.15% | 69.74 | 73.90% | 13.24% |
| 2 | 69.95% | 78.47% | 87.27% | 8.47% |

## *3.2 Nitrogen-Doped Boron Carbide Powder*

### 3.2.1 Powder Analysis

Samples 3 to 5 were prepared by mixing various amounts of N-doped powder with undoped powder as shown in Table 3.3.

**Tab** 3.3: Powder Description of Samples #3 - #5

| Sample # | Description |
|---|---|
| 3 | Mix of 37% $B_4C$, N addition, 98% C and 63% $B_4C$ |
| 4 | Mix of 50% $B_4C$, N addition, 98% C and 50% $B_4C$ |
| 5 | Mix of 63% $B_4C$, N addition, 98% C and 37% $B_4C$ |

$B_4C$ was identified as the main phase and graphite was identified as a secondary phase as shown in Figure 3.3. All patterns exhibit $B_4C$ peak broadening, indicative of nano-sized powder. $B_2O_3$ was identified in sample #5.

### 3.2.2 Sintering behavior

All samples displayed double-stage sintering as shown in Figure 3.4. Shrinkage onset began at 1850°C for all N-doped samples. A plateau occurred at 2100°C for all samples and sintering re-accelerated at 2250°C for all samples. All samples were soaked at 2400°C for two hours resulting in net shrinkage of 5.5% for samples #3 and #4 and 4% for sample #5.

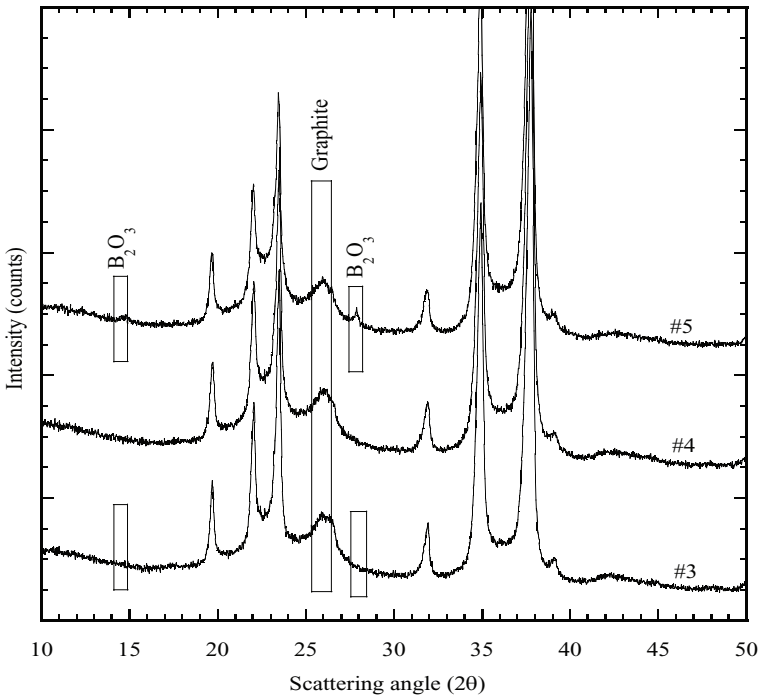


**Fig** 3.3: XRD peaks of nitrogen-doped PPG powders.

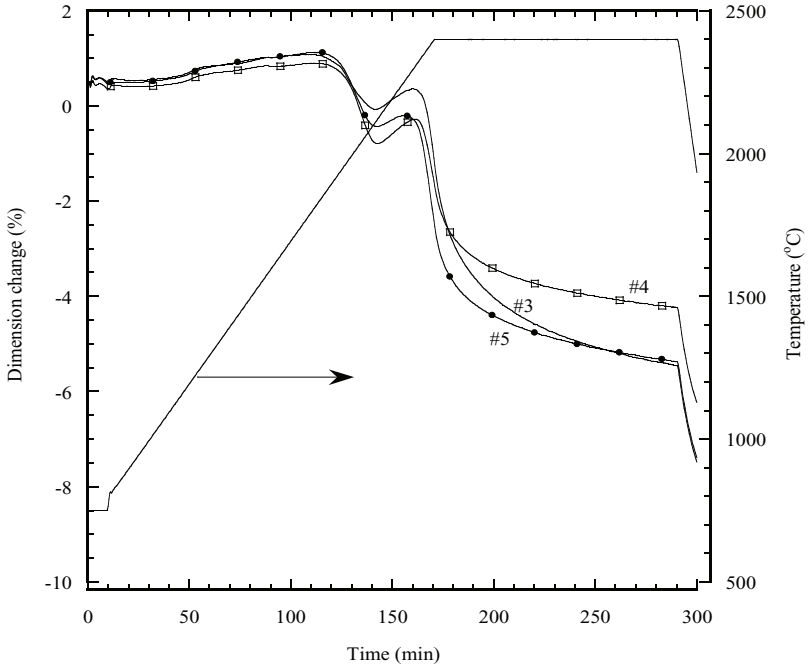


**Fig** 3.4: Dilatometer traces of nitrogen-doped PPG powders.

### 3.2.3 Density and Weight Loss

Nitrogen-doped powders had very low sintered densities as shown in Table 3.4.

**Tab** 3.4: Relative Density and Weight Loss of PPG #3 - #5.

| Sample number | Archimedes density (%) |
|---|---|
| 3 | 52.94% |
| 4 | 50.93% |
| 5 | 52.28% |

## *3.3 Iron-Doped Boron Carbide Powder*

### 3.3.1 Powder Analysis

Samples 6 to 11 were doped with various amounts of iron as shown in Table 3.5. The two lowest doped samples had additional carbon added and were purified.

**Tab** 3.5: Powder Description of Samples #6 - #11

| Sample # | Description |
|---|---|
| 6 | $B_4C$, 0.3% Fe, 98% C, purified |
| 7 | $B_4C$, 0.2% Fe, 98% C, purified |
| 8 | $B_4C$, 0.6% Fe |
| 9 | $B_4C$, 0.6% Fe |
| 10 | $B_4C$, 2.0% Fe |
| 11 | $B_4C$, 5.0% Fe |

$B_4C$ was identified as the main phase and graphite was identified as a secondary phase as shown in Figure 3.5. All patterns exhibit $B_4C$ peak broadening, indicative of nano-sized powder. Samples #10 and #11 exhibit a lower peak-to-noise ratio indicating a more amorphous nature than the other iron-doped samples. $B_2O_3$ was identified in all samples. There are unknown peaks at $\sim$17.5° and $\sim$18.5° in sample #6 and also at $\sim$11° and $\sim$12° in sample #11.

### 3.3.2 Sintering Behavior

All samples displayed double-stage sintering as shown in Figure 3.6. Shrinkage onset began at 1650°C for samples #6 and #9, at 1750°C for samples #7 and #8, and at 1600°C for

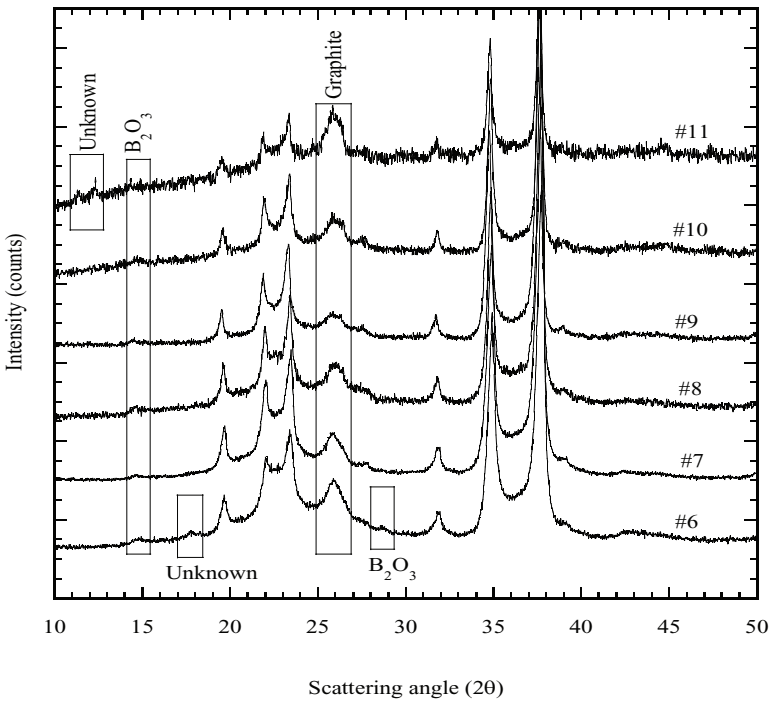


**Fig** 3.5: XRD peaks of iron-doped PPG powders.

samples #10 and #11. A plateau occurred at 2000°C for all Fe-doped samples except #11 which had a plateau at 1900°C. Shrinkage re-accelerated at 2100°C for samples #6, #9, #10 and #11, at 2200°C for sample #7, and at 2300°C for sample #8. Sample #6 was soaked at 2300°C for 30 minutes, sample #7 was soaked for 45 minutes, sample #8 was soaked for 90 minutes and samples #9, #10 and #11 were soaked for 60 minutes. The resulting net shrinkage was 7% for sample #6, 3% for sample #7, 3.5% for samples #8 and #10, and 6% for sample #9. Sample #11 experienced a large expansion at low temperature and no net shrinkage.

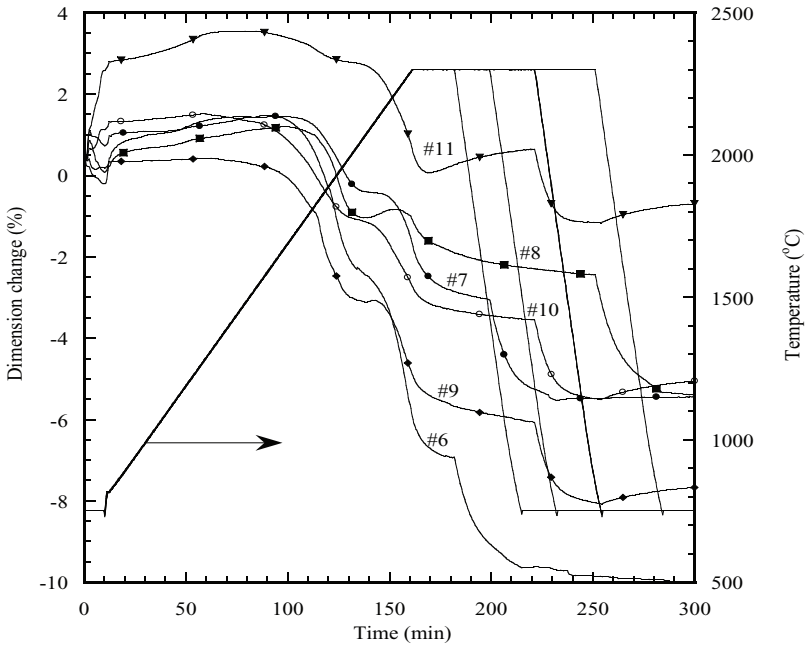


**Fig** 3.6: Dilatometer traces of iron-doped PPG powders.

### 3.3.3 Density and Weight Loss

Green densities ranging from ∼66.5% to greater than 71% resulted in an increase of density from ∼3% to 30% after sintering as shown in Table 3.6.

**Tab** 3.6: Relative Density and Weight Loss of PPG #6 - #11.

| Sample number | Green density (%) | Geometrical density (%) | Archimedes density (%) | Weight loss (%) |
|---|---|---|---|---|
| 6 | 66.50% | 83.00% | 86.52% | 10.90% |
| 7 | 67.49% | 74.31% | 75.68% | 11.46% |
| 8 | 66.47% | 67.52% | 71.90% | 16.28% |
| 9 | 71.60% | 87.90% | 89.92% | 7.60% |
| 10 | 71.15% | 79.95% | 83.97% | 10.24% |
| 11 | 67.09% | 66.73% | 68.99% | 15.56% |

## *3.4 Multiply-Doped Boron Carbide Powder*

### 3.4.1 Powder Analysis

Samples #12 to #20 are all doped with various amounts of iron and from one to six additional additives as shown in Table 3.7.

**Tab** 3.7: Powder Description of Samples #12 - #20

| Sample # | Description |
|---|---|
| 12 | $B_4C$, Fe and Si doped |
| 13 | $B_4C$, 0.3% Fe, 0.15% Si, 98% C, purified |
| 14 | $B_4C$, 0.1% Fe, 0.3% W |
| 15 | $B_4C$, 0.1% Fe, 0.3% W, 0.1% Ti |
| 16 | $B_4C$, 0.04% Fe, 0.03% Si, 0.04% Al, 0.03% Na, 0.01% Ti, 0.06% W |
| 17 | $B_4C$, 0.6% Fe, 0.3% Si, 0.06% Al, 0.02% Na, 0.1% Ti, 0.3% W, 0.06% Ca |
| 18 | $B_4C$, 0.6% Fe, 0.3% Si, 0.06% Al, 0.02% Na, 0.1% Ti, 0.3% W, 0.06% Ca, acid treated |
| 19 | $B_4C$, 0.6% Fe, 0.3% Si, 0.06% Al, 0.02% Na, 0.1% Ti, 0.3% W, 0.06% Ca |
| 20 | $B_4C$, 0.04% Fe, 0.03% Si, 0.04% Al, 0.03% Na, 0.01% Ti, 0.06% W, 0.02% Ca |

$B_4C$ was identified as the main phase and graphite was identified as a secondary phase as shown in Figure 3.7. All patterns exhibit $B_4C$ peak broadening, indicative of nano-sized

powder. $B_2O_3$ was identified in all samples. There are unknown peaks at ∼18° in samples #12, #13 and #20 and also at ∼27.5° in samples #13 and #20. These peaks may be silicon tetraboride ($SiB_4$) and quartz ($SiO_2$).

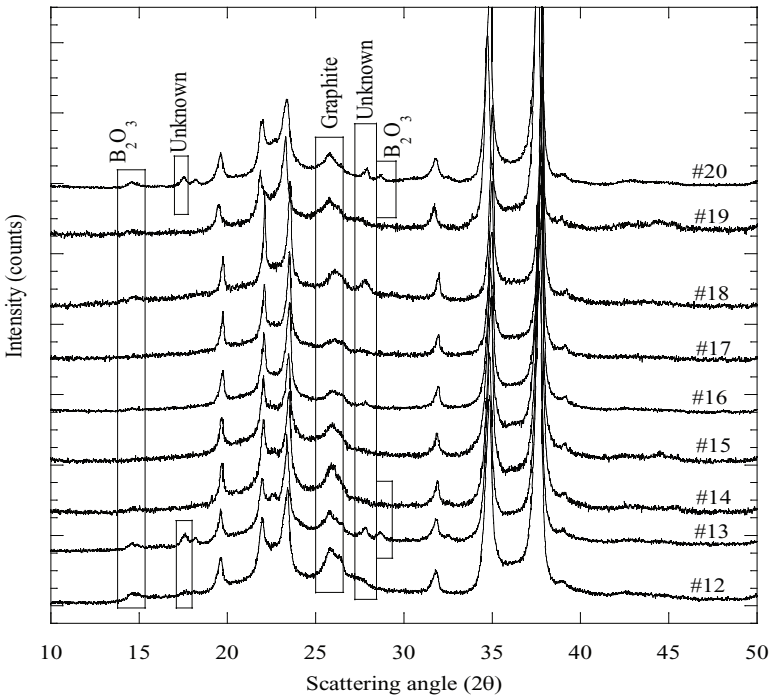


**Fig** 3.7: XRD peaks of multiply-doped PPG powders.

### 3.4.2 Sintering Behavior

Figure 3.8 shows the sintering behavior of samples doped with two or three dopants (#12 to #15) and Figure 3.9 shows the sintering behavior of samples doped with six or seven dopants (#16 to #20). All samples displayed double-stage sintering. Shrinkage onset began at 1750°C for samples #12 to #15, at 1700°C for samples #16 to #18 and at 1300°C for samples #19 and #20. A plateau occurred at 2000°C for all multiply-doped samples except #19 which experienced a plateau beginning at 1900°C. Shrinkage re-accelerated at 2200°C for all samples except #19 which re-accelerated at 2100°C. Samples #12, #13 and #19 were soaked at 2300°C for 90 minutes and samples #14, #16 to #18 and #20 were soaked for 60 minutes. The resulting net shrinkage was 6% for sample #12, 3% for samples #13, #14 and #19, 2% for samples #15 and #18, and 4% for samples #16, #17 and #20. Sample #19 experienced a large expansion at low temperature.

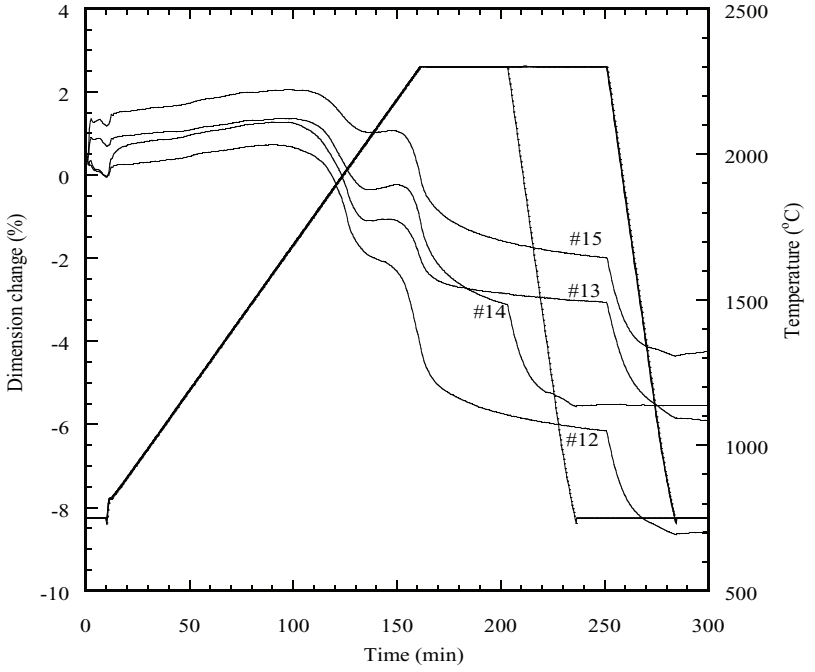


**Fig** 3.8: Dilatometer traces of two or three additive doped PPG powders.

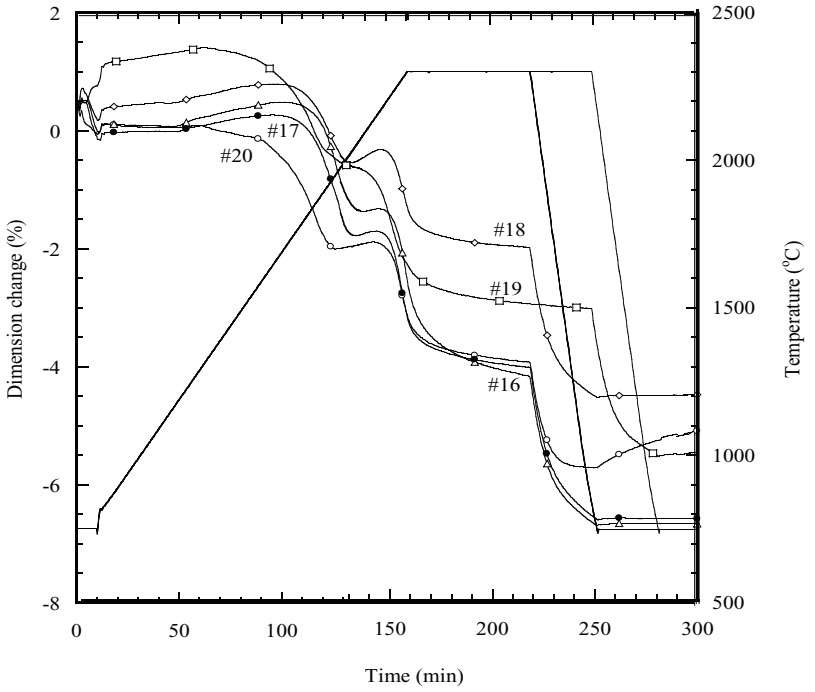


**Fig** 3.9: Dilatometer traces of six or seven additive doped PPG powders.

### 3.4.3 Density and Weight Loss

Green densities ranging from ∼64% to greater than 70% resulted in an increase of density from less than 1% to 27% after sintering as shown in Table 3.8.

**Tab** 3.8: Relative Density and Weight Loss of PPG #31 - #40.

| Sample number | Green density (%) | Geometrical density (%) | Archimedes density (%) | Weight loss (%) |
|---|---|---|---|---|
| 12 | 69.93% | | 87.26% | 8.54% |
| 13 | 66.83% | 73.65% | 75.11% | 12.24% |
| 14 | 66.25% | 64.48% | 66.84% | 12.37% |
| 15 | 63.87% | 71.94% | 75.51% | 11.24% |
| 16 | 64.05% | 72.12% | 73.88% | 10.09% |
| 17 | 64.18% | 69.09% | 71.22% | 14.18% |
| 18 | 65.78% | 65.38% | 67.83% | 17.67% |
| 19 | 68.77% | 83.02% | 86.14% | 5.97% |
| 20 | 70.43% | 81.49% | 89.70% | 7.85% |

## *3.5 Aluminum-Doped Boron Carbide Powder*

### 3.5.1 Powder Analysis

Samples #21 to #24 were doped with increasing amounts of aluminum as shown in Table 3.9. The low-doped sample was also purified and had additional carbon added.

**Tab** 3.9: Powder Description of Samples #21 - #24

| Sample # | Description |
|---|---|
| 21 | $B_4C$, 0.1% Al doped, 98% C, purified |
| 22 | $B_4C$, 0.5% Al |
| 23 | $B_4C$, 2.0% Al |
| 24 | $B_4C$, 5.0% Al |

$B_4C$ was identified as the main phase and graphite was identified as a secondary phase as shown in Figure 3.10. All patterns exhibit $B_4C$ peak broadening, indicative of nano-sized powder. $B_2O_3$ was identified and there are unknown peaks at ∼17.5° and ∼18.5° in sample #21.

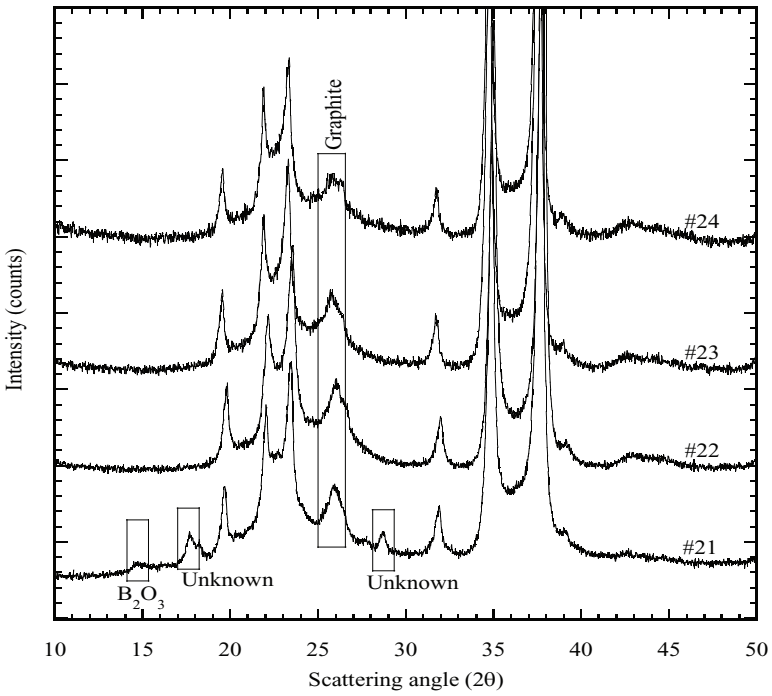


**Fig** 3.10: XRD peaks of aluminum-doped PPG powders.

### 3.5.2 Sintering Behavior

All samples displayed double-stage sintering as shown in Figure 3.11. Shrinkage onset began at 1700°C for sample #21, at 1500°C for samples #22 and #23 and at 1600°C for sample #24. A plateau occurred at 2000°C for all samples. Shrinkage re-accelerated at 2200°C for all samples. Sample #21 was soaked at 2300°C for 90 minutes, sample #22 was soaked for 30 minutes and samples #23 and #24 were soaked for 60 minutes. The resulting net shrinkage was 1.5% for sample #21, 8% for sample #22 and 6% for samples #23 and #24. Samples #23 and #24 experienced an unusual expansion behavior at low temperature.

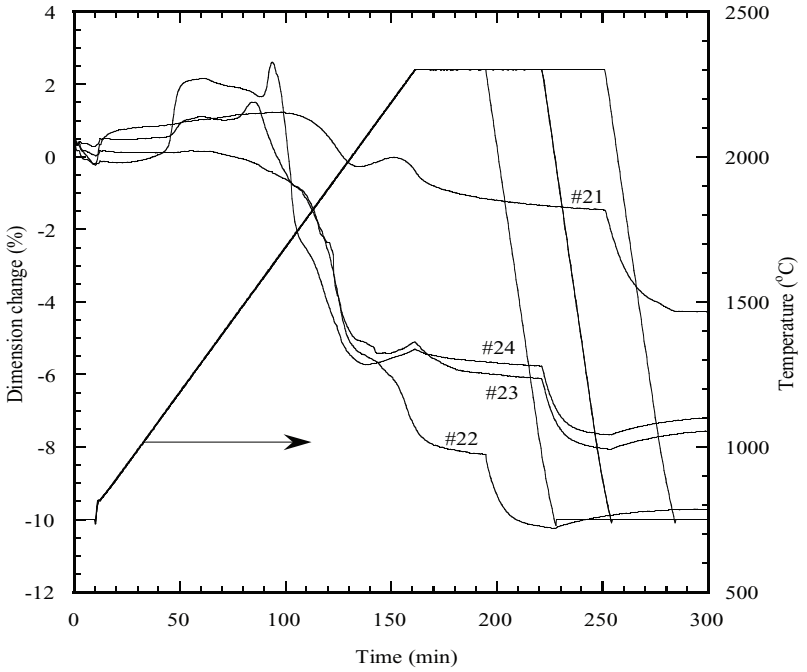


**Fig** 3.11: Dilatometer traces of aluminum-doped PPG powders.

### 3.5.3 Density and Weight Loss

Green densities ranging from ∼67% to greater than 70% resulted in an increase of density ∼9% to 34% after sintering as shown in Table 3.10.

**Tab** 3.10: Relative Density and Weight Loss of PPG #21 - #24

| Sample number | Green density (%) | Geometrical density (%) | Archimedes density (%) | Weight loss (%) |
|---|---|---|---|---|
| 21 | 66.73% | 71.07% | 72.72% | 12.40% |
| 22 | 71.08% | 90.75% | 94.81% | 7.66% |
| 23 | 69.26% | 85.67% | 88.60% | 12.71% |
| 24 | 68.24% | 68.41% | 80.53% | 19.89% |

## *3.6 Titanium-Doped Boron Carbide Powder*

### 3.6.1 Powder Analysis

Samples #25 to #28 were doped with increasing amounts of titanium as shown in Table 3.11.

**Tab** 3.11: Powder Description of Samples #25 - #28

| Sample # | Description |
|---|---|
| 25 | $B_4C$, 0.1% Ti |
| 26 | $B_4C$, 0.5% Ti |
| 27 | $B_4C$, 2.0% Ti |
| 28 | $B_4C$, 3.0% Ti |

$B_4C$ was identified as the main phase and graphite was identified as a secondary phase as shown in Figure 3.12. All patterns exhibit $B_4C$ peak broadening, indicative of nano-sized powder. $TiB_2$ peaks were also identified in samples #25 to #28.

### 3.6.2 Sintering Behavior

All samples displayed double-stage sintering as shown in Figure 3.13. Shrinkage onset began at 1700°C for all samples. A plateau occurred at 2000°C for all samples. Shrinkage re-accelerated at 2200°C for all samples. Sample #25 was soaked for 90 minutes and samples #26, #27 and #28 were soaked for 60 minutes. The net shrinkage increased from 5% to 8% as the amount of Ti increased. The lower doped Ti sample experienced some expansion at low temperature while the higher doped samples did not.

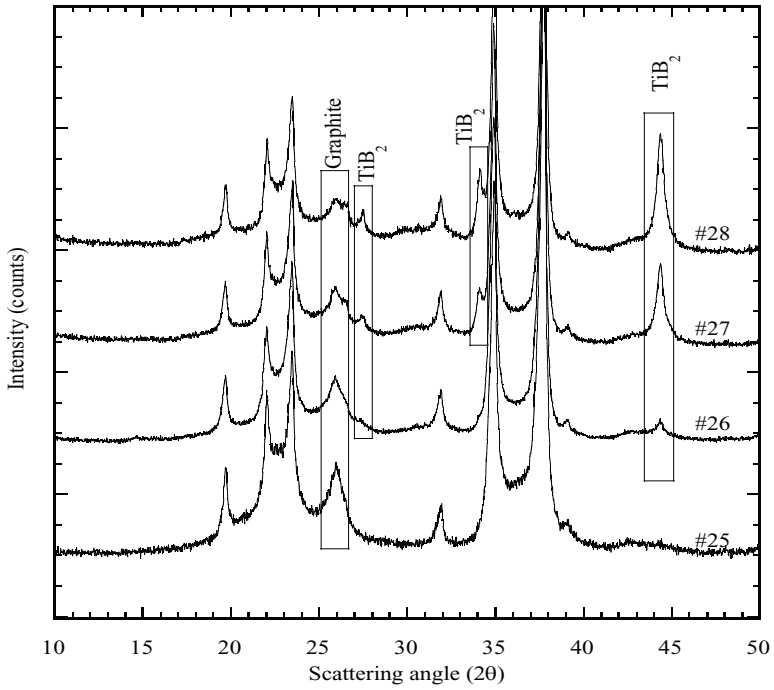


**Fig** 3.12: XRD peaks of titanium-doped PPG powders.

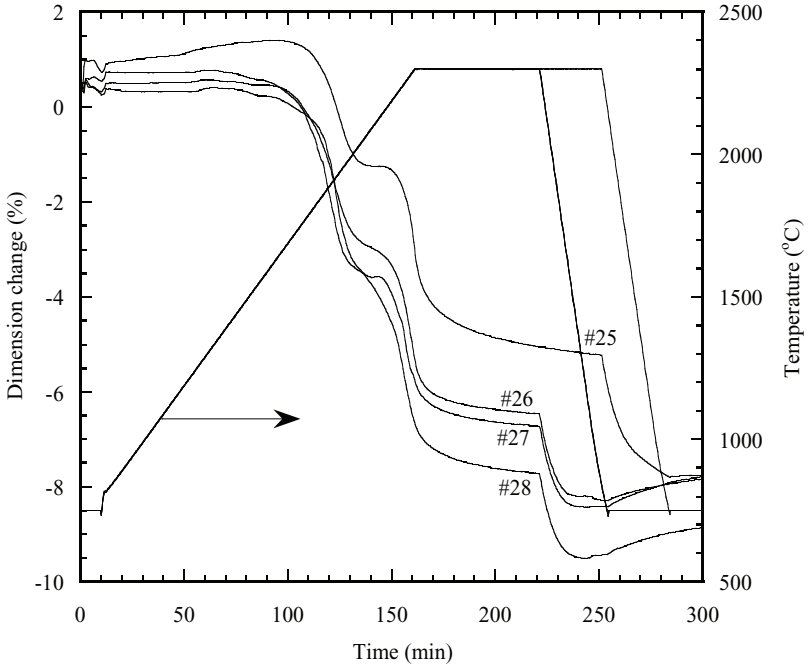


**Fig** 3.13: Dilatometer traces of titanium-doped PPG powders.

### 3.6.3 Density and Weight Loss

The three samples with green densities greater than 70% resulted in sintered densities greater than 91%, but the lower doped titanium sample had both low green density and low sintered density as shown in Table 3.12.

**Tab** 3.12: Relative Density and Weight Loss of PPG #25 - #28.

| Sample number | Green density (%) | Geometrical density (%) | Archimedes density (%) | Weight loss (%) |
|---|---|---|---|---|
| 25 | 60.79% | 75.85% | 77.80% | 10.87% |
| 26 | 70.93% | 88.59% | 91.57% | 7.66% |
| 27 | 70.27% | 87.32% | 91.45% | 7.61% |
| 28 | 70.50% | 92.86% | 94.68% | 8.97% |

## *3.7 Zirconium-Doped Boron Carbide Powder*

### 3.7.1 Powder Analysis

Samples 29 to 31 were doped with increasing amounts of Zirconium as shown in Table 3.13.

**Tab** 3.13: Powder Description of Samples #29 - #31

| Sample # | Description |
|---|---|
| 29 | $B_4C$, 0.5% Zr |
| 30 | $B_4C$, 2.0% Zr |
| 31 | $B_4C$, 5.5% Zr |

$B_4C$ was identified as the main phase. Graphite and $ZrB_2$ were identified as secondary phases as shown in Figure 3.14. A small amount of $B_2O_3$ remained in all samples. An unknown peak occurs at 17.5° in all samples.

### 3.7.2 Sintering Behavior

All samples displayed double-stage sintering as shown in Figure 3.15. Shrinkage onset increased as Zr amount increased from 1500°C to 1800°C. A plateau occurred at 2000°C for all samples. Shrinkage re-accelerated at 2100°C for all samples. All samples were soaked at 2300°C for 60 minutes. The net shrinkage was 8% for samples #29 and #31 and 7% for sample #30. Samples #30 and #31 an unusual expansion at low temperature.

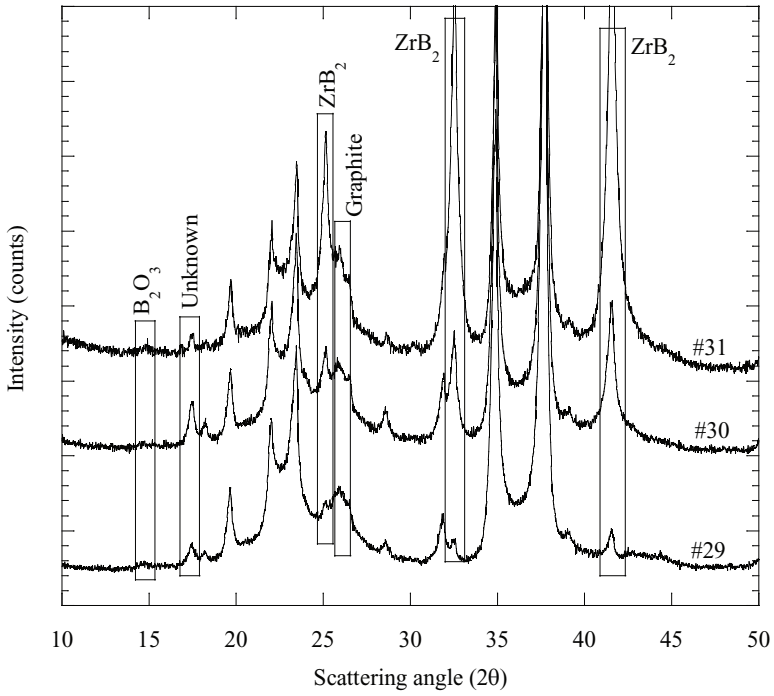


**Fig** 3.14: XRD peaks of zirconium-doped PPG powders.

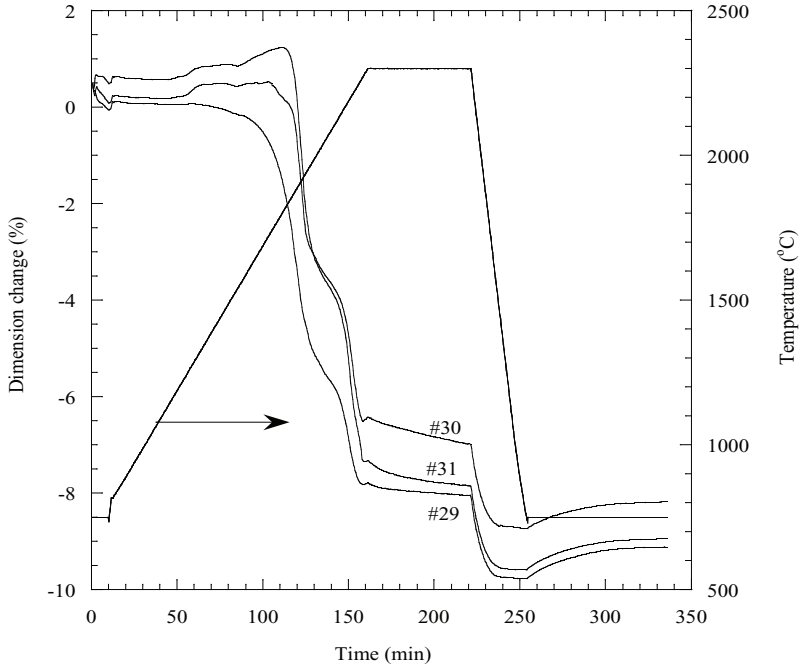


**Fig** 3.15: Dilatometer traces of zirconium-doped PPG powders.

### 3.7.3 Density and Weight Loss

Green densities greater than 69% resulted in sintered densities that increased with increased amounts of zirconium as shown in Table 3.14. All sintered samples had densities greater than 92%.

**Tab** 3.14: Relative Density and Weight Loss of PPG #29 - #52.

| Sample number | Green density (%) | Geometrical density (%) | Archimedes density (%) | Weight loss (%) |
|---|---|---|---|---|
| 29 | 69.13% | 88.94% | 92.12% | 7.88% |
| 30 | 68.68% | 89.84% | 92.69% | 10.41% |
| 31 | 72.84% | 89.84% | 93.50% | 14.02% |

## *3.8 Magnesium-Doped Boron Carbide Powder*

### 3.8.1 Powder Analysis

Samples 32 to 34 were doped with increasing amounts of magnesium as shown in Table 3.15.

**Tab** 3.15: Powder Description of Samples #32 - #34

| Sample # | Description |
|---|---|
| 32 | $B_4C$, 0.5% Mg |
| 33 | $B_4C$, 2.0% Mg |
| 34 | $B_4C$, 5.0% Mg |

$B_4C$ was identified as the main phase and graphite was identified as a secondary phase as shown in Figure 3.16. There are unknown peaks at ∼11° and ∼12° and at 17.5° in samples #33 and #34. MgO peaks were also identified.

### 3.8.2 Sintering Behavior

All samples experienced double stage sintering except #34 as shown in Figure 3.17. Shrinkage onset began at 1650°C for sample #32 and at 1800°C for samples #33 and #34. A plateau occurred at 2000°C for samples #32 and #33 and shrinkage re-accelerated at 2150°C. All samples were soaked at 2300°C for 120 minutes. The net shrinkage was 6% for sample #32, 8% for sample #33, and 5% for sample #34.

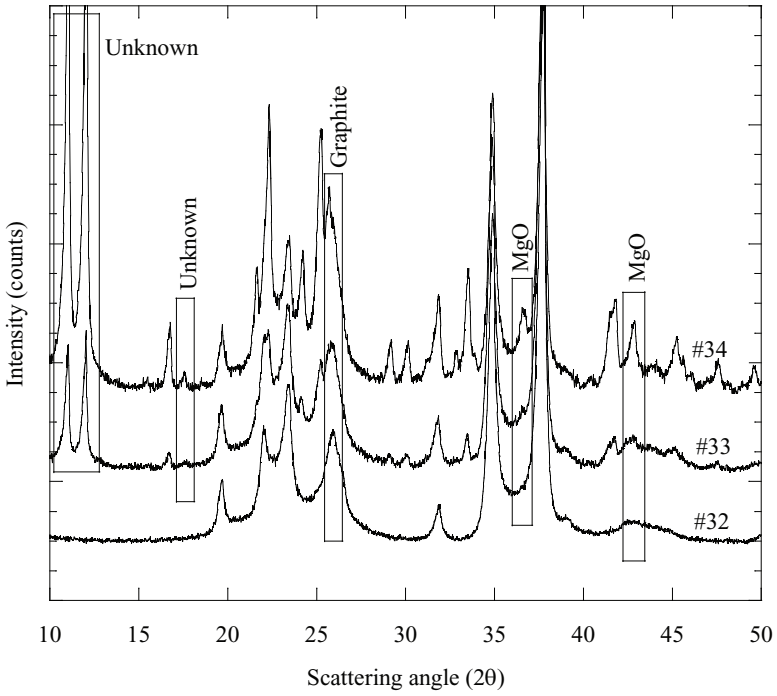


**Fig** 3.16: XRD peaks of magnesium-doped PPG powders.

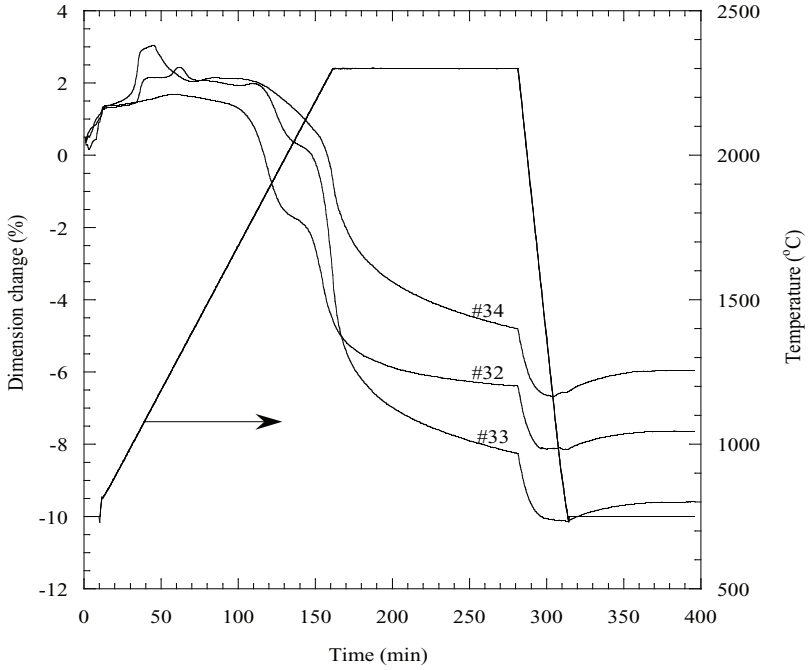


**Fig** 3.17: Dilatometer traces of magnesium-doped PPG powders.

### 3.8.3 Density and Weight Loss

Green densities of greater than 66% resulted in sintered densities of ∼85% and 79% for samples #32 and #33, respectively, as shown in Table 3.16. Sample #34 experienced a large weight loss and a lower sintered than green density.

**Tab** 3.16: Relative Density and Weight Loss of PPG #32 - #34.

| Sample number | Green density (%) | Geometrical density (%) | Archimedes density (%) | Weight loss (%) |
|---|---|---|---|---|
| 32 | 66.67% | 80.21% | 84.95% | 9.91% |
| 33 | 66.21% | 75.31% | 79.02% | 19.55% |
| 34 | 60.81% | 47.61% | 50.42% | 41.03% |

## *3.9 Tungsten-Doped Boron Carbide Powder*

### 3.9.1 Powder Analysis

Samples 35 to 38 were doped with increasing amounts of tungsten as shown in Table 3.17.

**Tab** 3.17: Powder Description of Samples #35 to #38

| Sample # | Description |
|---|---|
| 35 | $B_4C$, 0.3% W |
| 36 | $B_4C$, 0.5% W |
| 37 | $B_4C$, 2.0% W |
| 38 | $B_4C$, 5.0% W |

$B_4C$ was identified as the main phase and graphite was identified as a secondary phase as shown in Figure 3.18. All patterns exhibit $B_4C$ peak broadening, indicative of nano-sized powder. $WB_2$ peaks were also identified as a secondary phase with peaks increasing as amount of W increased. An unknown peak was identified at 17.5° in samples #36 to #38. Graphite peaks decreased in intensity as W dopant amount increased.

### 3.9.2 Sintering Behavior

All samples displayed double-stage sintering as shown in Figure 3.19. Shrinkage onset began at 1600°C for samples #35 to #37 and at 1800°C for sample #38. A plateau occurred at 2000°C for all samples. Shrinkage re-accelerated at 2200°C for all samples. Sample #35

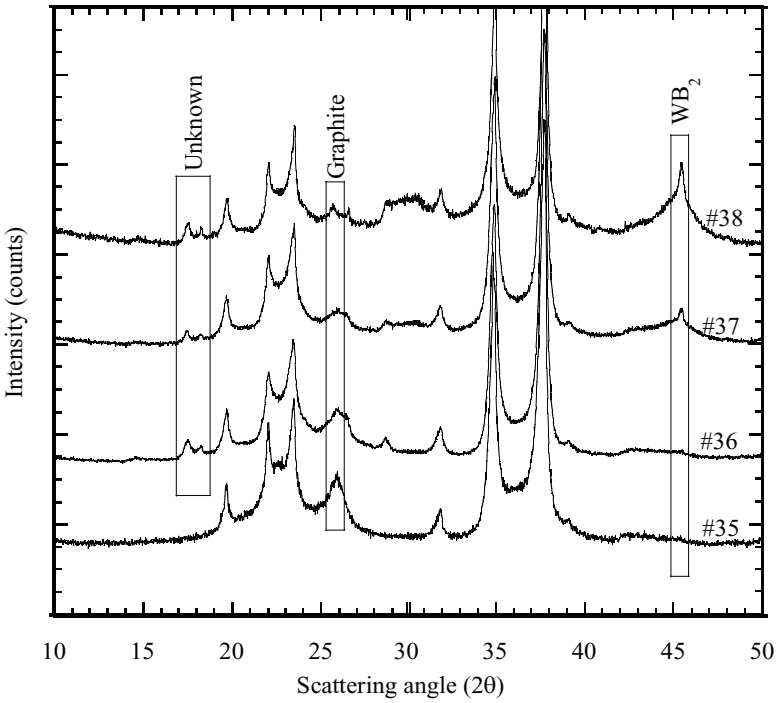


**Fig** 3.18: XRD peaks of tungsten-doped PPG powders.

was soaked at 2300°C for 45 minutes and samples #36, #37 and #38 were soaked for 60 minutes. The net shrinkage was 4.5% for sample #35, 7% for samples #36 and #38 and 8% for sample #37. Sample #35 experienced a large expansion at low temperatures and sample #38 experienced an unusual expansion beginning at 1550°C.

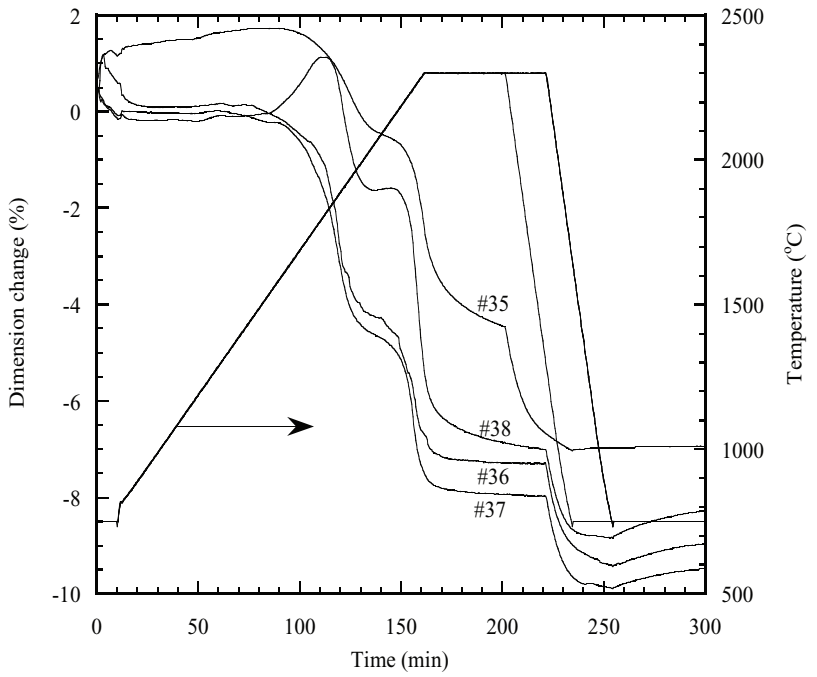


**Fig** 3.19: Dilatometer traces of tungsten-doped PPG powders.

### 3.9.3 Density and Weight Loss

The three samples with green densities greater than 68% resulted in sintered densities greater than 90%, but the low doped tungsten sample had both low green density and low sintered density as shown in Table 3.18.

**Tab** 3.18: Relative Density and Weight Loss of PPG #35 - #38.

| Sample number | Green density (%) | Geometrical density (%) | Archimedes density (%) | Weight loss (%) |
|---|---|---|---|---|
| 35 | 64.21% | 76.70% | 78.50% | 9.39% |
| 36 | 68.09% | 84.48% | 90.37% | 9.43% |
| 37 | 70.82% | 92.65% | 94.99% | 7.05% |
| 38 | 70.42% | 87.16% | 92.95% | 10.13% |

# CHAPTER 4

## Discussion

The nano-grained powders supplied by PPG Industries exhibits $B_4C$ peak broadening as shown in XRD data. Graphite peaks varied from powder to powder. For example, graphite peak trends decreased as dopant amounts increased for Ti and W, but the reverse occurred for increasing amounts of Mg.

Previous work in our lab [23] indicated the importance of removing $B_2O_3$ coatings from $B_4C$ powder. This was accomplished by soaking powder compacts at 1350° C in a hydrogen atmosphere. Any hydrogen remaining in the furnace after this soak would have deleterious effects on $B_4C$ sintering, therefore it was important to ensure removal of all hydrogen from the furnace before continuing the sintering process. For PPG nanopowders, methanol washing (repeated until a terminal weight was achieved) removed most of the $B_2O_3$ coatings, eliminating the need for hydrogen gas during sintering. Some residual $B_2O_3$ remained, likely due to poor contact between the methanol and $B_2O_3$ within agglomeration interiors. This residual oxide was volatized in the temperature range of 1150-1440°C, as noted by expansion humps in the dilatometer traces of many samples within this range.

The predicted lower sintering onset temperature was not realized with most samples. By methanol washing to remove $B_2O_3$, it was hoped that onset would occur around 1380°C. This onset temperature was observed in carbon doped (via phenolic resin) $B_4C$, likely as a result of the carbon reacting with and removing the $B_2O_3$ coatings. In N-doped samples, sintering onset occurred at temperatures as high as 1850°C. This is the temperature observed in pure $B_4C$ with an average grain size of 0.8 microns. Sintering onset for the remaining samples varied from 1300°C for two multiple-doped samples to 1800°C for several other samples. The average relative density of samples that experienced sintering onset at or below 1650°C was 86.8%, but for samples that experienced sintering onset above 1650°C,

the average relative density was 71.4%. A probable cause for the delay in sintering onset is the remaining $B_2O_3$ preventing direct contact between $B_4C$ particles until it is volatized at 1500°C. However, in the majority of samples, the beginning of densification still did not occur until a higher temperature was reached. This is likely due to the graphite coatings on the $B_4C$ particles that continued to prevent direct particle contact even after the removal of residual $B_2O_3$. Sintering onset temperature generally increases as the melting temperature of constituents increase [24]. Because graphite is more refractory than $B_4C$, sintering would start at a higher temperature than when $B_4C$ particles are in direct contact. The only powder that appeared to show a trend in sintering onset was Zr doped powder in which sintering onset temperature increased with increasing amounts of Zr.

Double-stage sintering is common in nano-$B_4C$. Solid state sintering first occurs when particles fall into the gaps created after volatilization of $B_2O_3$. This is followed by a brief plateau where shrinkage is slowed, stopped or reversed. Finally, a reaccelerated contraction occurs that corresponds to a coarser, interconnected liquid phase. The plateau results from the formation of larger grains from a presumably liquid phase and occurred in the range of 1900°C to 2100°C, occurring most often at 2000°C. According to the phase diagram, a liquid phase is not expected until around 2375°C. It is likely that the high surface energy of the nanopowder drove down the eutectic melting temperature thereby forming isolated droplets due to the fusion of collected nanoparticles. These isolated droplets were an order of magnitude larger than surrounding nanoparticles, resulting in rapid resolidification of the droplets even as heating increased. In general, liquid phase formation should not arrest contraction as observed with our samples. It is likely that since liquid phase was only present for a short period, the larger resolidified regions drew away from the nanoparticles and formed air gaps that hindered sintering.

Re-accelerated sintering occurred in the samples anywhere from 2100°C to 2300°C, occurring most often at 2200°C. This resumed contraction resulted from the formation of a substantially interconnected liquid phase that remained even as the temperature increased. This interconnected liquid phase created a capillary action that drew liquid into open pores and/or facilitated slumping, both of which lead to rapid densification. The liquid still

formed below the 2375°C eutectic perhaps due to unknown impurities either noted as such on XRD diagrams or not detected by XRD. However, an older phase diagram [24] indicates a eutectic at 30 wt% carbon occurring at 2160°C which is in good agreement with our study.

Final sintered relative densities ranged from 50% to more than 95%. The low sintered density obtained for the nitrogen-doped samples (less than 53%) is likely due to the higher soaking temperature. Work done in our lab previously has indicated that soak temperatures greater than 2320°C, leads to degradation in both density and hardness likely due to rapid grain growth and decomposition of the $B_4C$ phase.

Shrinkage amount appeared to be directly tied to final relative density, although there were a couple of exceptions. For example, all samples with final relative densities greater than 93% experienced shrinkage of at least 7%, but both an Fe-doped and a Mg-doped sample had this amount of shrinkage and had much lower final densities. Both the Zr and the Ti-doped samples experienced increased densities as the amount of dopant increased, but the reverse was true for the Mg-doped samples. This reverse trend in the Mg samples may be due to the increasing amount of the unknown contamination that showed up in the XRD data at 11° and 12°. XRD data for sintered samples with greater than 93% relative densities show sharper peaks in general and greater intensity of graphite peaks compared to their as-received diffraction patterns as shown in Figure 4.1. 93% is considered the critical density necessary to achieve theoretical density through post-HIPing.

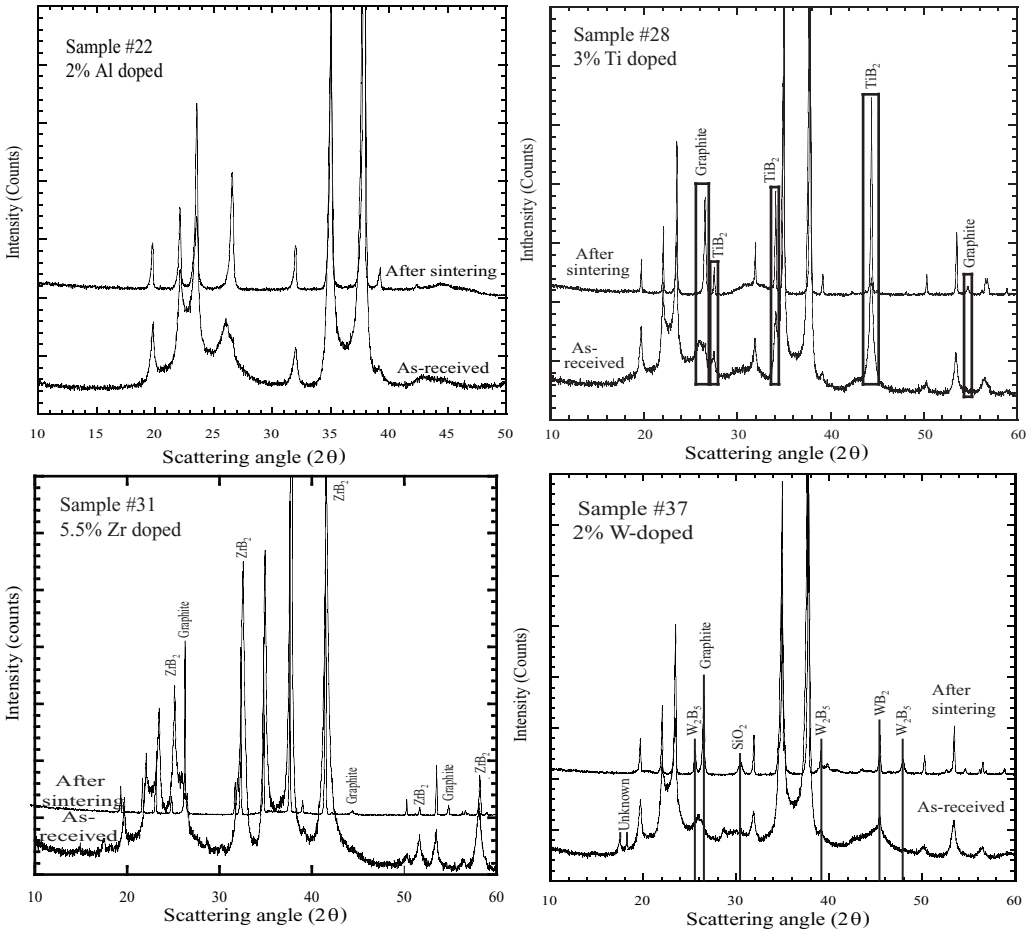


**Fig** 4.1: Comparison of XRD data for high sintered density samples.

It was expected that hot isostatic pressing of samples sintered to greater than 93% relative density would increase relative density to 100%. This was not realized in any of the post-HIPed samples. Post-HIP density only improved slightly as shown in Table 4.1. Nano-sized ceramic powders have been shown to experience excessive grain growth when densities of greater than 90% are achieved. It is believed this is due to the closing of any remaining open pores, thus greatly increasing pore mobility. With increased mobility, the pores no longer function as pinning centers for grain boundaries [19].

The micrograph of sample #22 shown in Figure 4.2 indicates an inhomogeneous surface area.

**Tab** 4.1: Sintered and Post-HIP Relative Density

| Sample number | Sintered relative density (%) | Post-HIP relative density (%) |
|---|---|---|
| 22 | 94.81% | 96.22 |
| 28 | 94.68% | 97.03% |
| 31 | 93.50% | 94.88% |
| 37 | 94.99% | 98.45% |

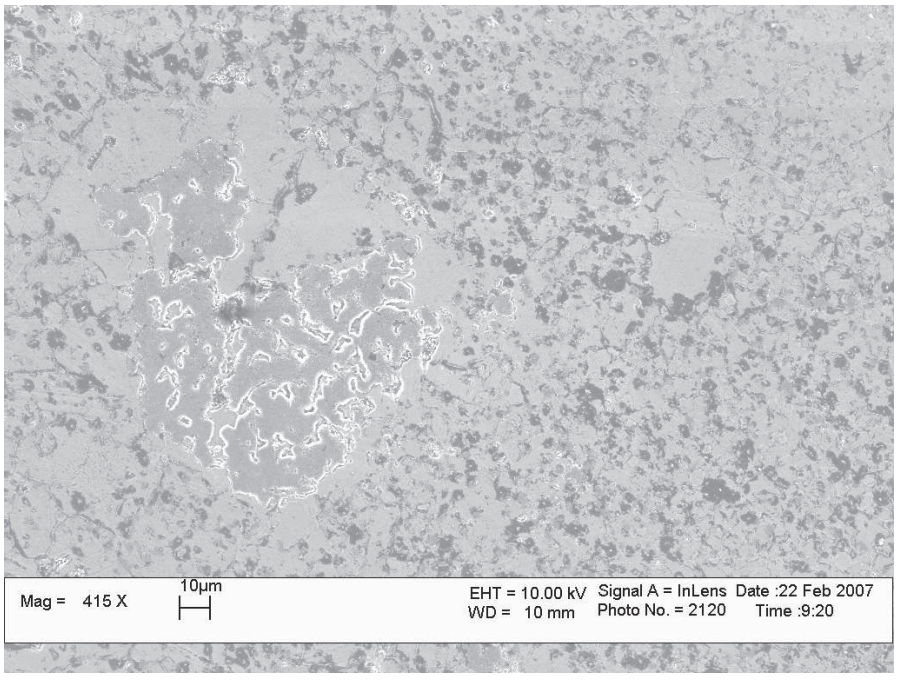


**Fig** 4.2: Micrograph of post-HIP sample #22.

# CHAPTER 5

## Conclusion

The study of nanopowder carbides, particularly $B_4C$, is still a fairly new field and there is much to understand about the sintering mechanics of these powders. In this preliminary study, we have shown that $B_2O_3$ can be removed effectively with methanol washing and any residual $B_2O_3$ can be removed during normal sintering processes, eliminating the need for a hydrogen soak inside a furnace. It appears that the anticipated sintering onset temperature of less than 1500°C may not be possible. However, there are still advantages of using nanopowders, such as increased strength with decreased grain size and potential superplasticity that should offset this shortcoming. We have also shown that sintered densities up to 95% can be achieved with the addition of various dopants, though post-HIP densities were lower than expected.

Future work includes conducting hardness analysis on post-HIP samples and comparing these results to sintered samples of the same composition as well as accepted values for standard boron carbide powders. SEM analysis on these samples should also prove useful in determining why the desired post-HIP density of 100% was not obtained in any of the samples that reached a sintered density greater than 93%. This will, hopefully, lead to information that will allow 100% post-HIP density to be obtained.

# REFERENCES


[1] J. F. Shackelford and W. Alexander, *CRC Materials Science and Engineering Handbook*, CRC Press, Boca Raton, Fl., 1991.

[2] F. Thevenot, "A Review on Boron Carbide," *Key Engineering Materials*, **56-57** 59-88 (1991).

[3] F. Thevenot, "Boron Carbide-A Comprehensive Review," *Journal of the European Ceramic Society*, **6** [4] 205-225 (1990).

[4] H. Pierson, *Handbook of Refractory Carbides and Nitrides: Properties, Characteristics, Processing and Applications*, Noyes Publishing, Westwood, NJ, 1996.

[5] D. Emin, "Structure and Single-Phase Regime of Boron Carbides," *Physical Review B*, **38** 6041-55 (1988).

[6] M. L. Wilkins and R. L. Landingham, "Prologue: Fifth Progress Report on Light Armor Program," *Internation Journal of Applied Ceramic Technology*, **1** [3] 203-204 (1969).

[7] J. W. McCauley and D. J. Viechnicki, "Ceramics R & D at the U. S. Materials Technology Lab," *American Ceramic Society Bulletin*, **70** [8] 1340-1344, (1988).

[8] R. F. Speyer and H. Lee, "Advances in Pressureless Densification of Boron Carbide," *Journal of Materials Science*, **39** 6014-6021 (2004).

[9] H. Kim, Y. Young and H. E. Kim, "Densification and Mechanical Properties of $B_4C$ with $Al_2O_3$ as a Sintering Aid," *Journal of the American Ceramic Society*, **83** (2000).

[10] V. Skorokhod, Jr., M. D. Vlajic, and V. D. Krstic, "Mechanical Properties of Pressureless Sintered Boron Carbide Containing $TiB_2$ Phase," *Journal of Materials Science Letters*, **15** [15] 1337-39 (1996).

[11] K. Schwetz, W. Grellner and A. Lipp, "Mechanical Properties of HIP Treated Sintered Boron Carbide," *Institute of Physics Conference Series*, [75] 413-426 (1986).

[12] S. Yamada, S. Sakaguchi, K. Hirao, Y. Yamauchi and S. Kanzaki, "Mechanical Properties of Boron Carbide Ceramics," *Ceramic Engineering and Science Proceedings*, **22** [3] 215-220 (2001).

[13] Z. Zakhariev and D. Radev, "Properties of Polycrystalline Boron Carbide Sintered in the Presence of $W_2B_5$ without Pressing," *, Journal of Materials Science Letters*, **7** [7] 695-96 (1988).

[14] N. Cho, Z. Bao, and R. F. Speyer, "Density and Hardness-optimized Pressureless Sintered and Post-hot Isostatic Pressed $B_4C$," *Journal of Materials Research*, **20** [8] 2110-16 (2005).

[15] R. Vaben and D. Stover, "Processing and Properties of Nanophase Non-oxide Ceramics," *Materials Science and Engineering A*, **301** [1] 59-68 (2001).

[16] J. R. Groza and R. J. Dowding, "Nanoparticulate Materials Densification," *Nanostructured Materials*, **7** [7] 749-768 (1996).

[17] R. Averback, H. Hoffler, H. Hahn and J. Logas, "Sintering and Grain Growth in Nanocrystalline Ceramics," *Nanostructured Materials*, **1** [2] 173-8 (1992).

[18] O. Vasylkiv, Y. Sakka, and V. V. Skorokhod, "Low-temperature Processing and Mechanical Properties of Zirconia and Zirconia-Alumina NanoCeramics," *Journal of the American Ceramic Society*, **86** [2] 299-304 (2003).

[19] R. Vaben and D. Stover, "Processing and Properties of Nanophase Ceramics," *Journal of Materials Processing Technology*, **92** 77-84 (1999).

[20] R. Rice, "Effects of Environment and Temperature on Ceramic Tensile Strength-grain Size Relations," *Journal of Materials Science*, vol. 32, pp. 3071-87, 1997.

[21] B. Kim, K. Hiraga, K. Morita, and S. Sakka, "A High-strain-Rate Superplastic Ceramic," *Nature*, **413** [6853] 288-91 (2001).

[22] X. Xu, T. Nishimura, N. Hirosaki, R. Xie, Y. Yamamoto, and H. Tanaka, "Superplastic Deformation of Nano-sized Silicon Nitride Ceramics," *Acta Materialia*, **54** 255-262 (2006).

[23] H. Lee, W. Hackenberger, and R. Speyer, "Sintering of Boron Carbide Heat-treated with Hydrogen," *Journal of the American Ceramic Society*, **85** [8] 2131-2133 (2002).

[24] N. Cho, K. Silver, Y. Berta, R. Speyer, N. Varnier and C.-H. Hung "Densification of Carbon-Rich Boron Carbide Nanopowder Compacts," *Journal of Materials Research*, **22** [5] 1354-1359 (2007).